PROBABILITY AND STATISTICAL MODELING: TI-6AL-4V PRODUCED VIA DIRECTED ENERGY DEPOSITION

Peter C. Collins
Department of Materials Science and Engineering
Iowa State University
2240 Hoover Hall
Ames, IA 50011, U.S.A.
pcollins@iastate.edu
515-294-5127

D. Gary Harlow
Department of Mechanical Engineering and Mechanics
Lehigh University
19 Memorial Drive West
Bethlehem, PA 18015, U.S.A.
dgh0@lehigh.edu
610-758-4127

Abstract:

Additive manufacturing is a complex multi–parameter process. Electron beam additive manufacturing of titanium (Ti-6Al-4V), which consists of a multitude of layers of deposited metal, exhibits significant variability in many key aspects including composition, microstructure, and mechanical properties. When establishing methods to predict material properties of these builds, it is necessary to consider both geometry and microstructure. Specifically, the material property of interest is the yield stress. The constitutive equation that is used to predict the yield stress of specimens subjected to stress relief annealing in the $\alpha+\beta$ phase field has been developed previously. The yield stress equation contains random variables which are modeled with appropriate cumulative distribution functions that characterize their statistical observations. Subsequently, these distributions functions are incorporated into the physically based model using

standard simulation techniques. The main purpose of this integrated modeling and statistical analysis is to begin to characterize the yield stress, especially in the extreme lower tail which is critical for high reliability estimation and prediction. To manage uncertainty and improve the estimation of the yield stress, an established methodology for calibration of the distribution function for the yield stress using experimental data is applied.

1. Introduction

Research and publications into metal-based Additive Manufacturing (AM) has increased significantly over the past 2 decades, increasing from fewer than 40 articles/year in 1999 to >23,000 articles/year in 2020. The fundamental research has been expansive – ranging from seminal papers focusing on fundamental physics of the AM processes [1-5] to the resulting compositions and microstructures [6-11] and properties [12,13] of various AM methods. Other researchers have explored the possibilities of producing compositionally or microstructurally graded structures [14-17] for either exploration of composition-microstructure relationships and/or alloy development [18] or for potential applications. Still other researchers have explored the possibility of in-situ analysis of depositions using either high-energy beamlines [19-24] or nondestructive evaluation methods using known modalities [25,26]. However, in the main, there are still gaps in the published literature. These include: (i) techniques to predict the performance of AM materials; (ii) robust and well-exercised Integrated Computational Materials Engineering (ICME) models to link composition and process information through microstructure/defect structures and to properties and performance, including the possibility to predict properties and performance in compositionally graded structures; (iii) techniques to measure and quantify the

materials state[1] [27,28] during deposition and/or at appropriate length scales; and (iv) the possibility of tailoring/controlling the materials state during the AM process. This paper seeks to directly address the first of these gaps and demonstrate a strategy to build upon models that can predict properties given a certain composition/microstructure – and predict the resulting expected performance of a given part, as defined by a probability distribution function of properties. This paper also seeks to demonstrate the techniques to translate a property-prediction model into a validated model to predict the probability and statistics of a given property for a large-area additive manufacturing approach that is of interest to the aerospace sector for its ability to produce large metallic structures.

A variant of directed energy deposition, specifically electron beam additive manufacturing (EBAM), was used to produce four relatively large-scale and geometrically identical notional parts, designated as NP1, NP2, NP3, and NP4B; see Fig. 1. These parts were sectioned for microstructural characterization and tensile testing. Because of the geometry of the deposition eight different orientations have been considered from which uniaxial tensile specimens have been machined (see Fig. 2). The orientations, shown in Fig. 2, are as follows:

x – along the build path of the deposited beads,

y – normal to the deposited beads in the same plane as deposition,

z – normal to both the deposited beads and the plane containing x and y,

xc – in the plane of deposition where deposited beads crisscross,

zc – normal to the plane of deposition where deposited beads crisscross,

[1] According to the seminal publications on the concept of Materials State by E. Lindgren and J. Aldrin, they define Materials State Awareness (MSA) as "Digitally Enabled Reliable Nondestructive Quantitative Materials / Damage Characterization Regardless of Scale"

I – normal to the plane of deposition where the specimen contains the interface between the plate and the deposit,

k – 45° in the y – z plane, and

kc – 45° in the y – z plane where deposited beads crisscross.

Materials characterization was completed for the specimens obtained from NP1, NP2, and NP3. Using those data, a scientifically and empirically based model was developed to characterize the yield stress σ_{YS} [13]. Building upon this model, the first part of this paper is to statistically characterize the cumulative distribution functions (cdfs) for the key material properties used in the model. The second step is to incorporate the cdfs for the material properties into a simulation algorithm to estimate σ_{YS}. Confidence bounds using mean square error (MSE) and mean absolute error (MAE) are also estimated for the model. To calibrate the model, the third procedure is to use the DARPA Open Manufacturing Approach (a variant of the DARPA Accelerated Insertion of Materials (AIM) approach [29]) to calibrate the model using the σ_{YS} data from NP1, NP2, and NP3. Finally, the calibrated model is used to estimate the behavior of the σ_{YS} data from NP4B blindly, that is, without any data used from NP4B. This final step serves as validation that the methodology is sound and warranted for further applications.

2. Statistical Characterization of Material Properties

The subsequent analyses are for the additive manufactured $\alpha+\beta$ stress relived (AMSR) conditions [30]. Based upon previous modeling and experimentation, there are nine key material variables that need to be statistically characterized [31-35]. This includes four compositional variables (Al, V, O, Fe) and five microstructural variables (volume fraction alpha, volume fraction colony, colony scale factor, alpha lath width, and beta rib thickness). These variables are also

shown in Table 1. Thus, the compositions of the elements Al, O, Fe, and V are critical to the analysis presented here. Importantly, this does not exclude the role of other elements on strengthening mechanisms (*e.g.*, N, C, and H) which are known to exhibit a strong influence on properties, but for which the physical terms to include in the models are unknown, as are discrete measurements in these datasets, although it is known that, on average, their concentration is low. Figure 3 shows the data for the composition of Al plotted on normal probability paper. Note that if the data are linear, then a normal cdf is a good characterization of that data. The data are for all orientations considered. The sample size is 78. As indicated by the linear regression, the normal cdf is an excellent representation of these data. This observation is also confirmed using maximum likelihood estimation (MLE) and the Kolmogorov-Smirnov (KS) and Anderson-Darling (AD) goodness-of-fit tests [36]. The estimated mean μ and standard deviation σ are 5.697 and 0.131, respectively. Both μ and σ can be estimated from the slope and intercept from the linear regression through the data. The regression analysis also confirms that the estimated cdfs are acceptable because the correlation coefficient is 0.994 which is quite close to unity. These observations are qualitatively the same for the concentration of V. Figure 4 is similar to Fig. 3 for the V data. The correlation coefficient is 0.959 which is indicates that the estimated cdf is acceptable. Table 1 contains all the random variables, the cdf used for their characterization, and the appropriate parameters.

The concentrations for Fe and O are discrete, *i.e.*, there are basically only two values for them, which are denoted as the minimum (min) and maximum (max) in Table 1. Consequently, they are estimated by the fraction of observations for each value. For example, the concentration of O is equal to 0.165 for 60 observations and 0.169 for 22 observations. Thus, the estimated fractions are

60/82 and 22/82, respectively. Again, the concentration for Fe behaves similarly. See Table 1 for the estimated values.

There are five other random variables that need to be characterized. These are the alpha volume fraction F_V^{α}, the colony volume fraction F_V^{colony}, the alpha lath width $t_{\alpha-lath}$, the beta rib width $t_{\beta-rib}$, and colony scale factor t_{colony}. While the first four are widely understood for titanium microstructures, the fifth may be less well known. Colony scale factor is a measure of the size of a colony, analogous to grain size, but with the term factor used as we do not know *a priori* the shape of the colony (or grain) in three-dimensions, and hence, we cannot calculate a true size using any stereological technique. The first four of these can be acceptably characterized by a normal cdf. The appropriate cdfs are included in Table 1. The colony scale factor t_{colony} has a different statistical character. Figure 5 shows all the t_{colony} data from NP1, NP2, and NP3. A three parameter Weibull cdf is given below:

$$F(x) = 1 - \exp\{-[(x-\gamma)/\beta]^{\rho}\}, \quad x \geq \gamma, \tag{1}$$

where ρ is the shape parameter, β is the scale parameter, and γ is the minimum value. This cdf is acceptable to represent these data. The KS test indicates that the cdf is acceptable for any significance less than 20%. The AD test, however, implies that the cdf is acceptable only for a significance of 1%. This is directly attributable to the difference in the lower tail of the data. Nevertheless, these cdfs will be used, herein.

3. Yield Stress Model

The random variables above serve as the critical variables in a physically based model developed and investigated in [13]. The development of the model was built upon the data obtained from NP1, NP2, and NP3. The equation for σ_{YS} is as follows:

$$\sigma_{YS} = \left\{ \begin{bmatrix} \left(F_V^{\alpha}\sigma_o^{\alpha} + F_V^{\beta}\sigma_o^{\beta}\right) + \left(F_V^{\alpha}\sigma_{SS}^{\alpha} + F_V^{\beta}\sigma_{SS}^{\beta}\right) + F_V^{colony} C_{\alpha-lath}\left(t_{\beta-rib} / t_{\alpha-lath}\right)^{0.5} \\ + F_V^{colony} C_{colony} t_{colony}^{-0.5} + \left(t_{colony} / t_{\alpha-lath}\right) + F_V^{BW}\alpha MGb\sqrt{\rho} \end{bmatrix} \right\} AxisDebit, \quad (2)$$

where the first term corresponds to the intrinsic strength, the second is for solid solution strengthening, the third is a Hall-Petch strengthening term for α-laths, the fourth is a Hall-Petch strengthening term for colonies, the fifth term represents the interfacial strength (which can help to account for interfaces which act as barriers for dislocation transmission), and the last term in the summation characterizes the active Taylor hardening. The factor outside of the square bracket labeled *AxisDebit* accounts for known effects based upon different uniaxial tensile specimen orientations. For further details see [13]. It is nontrivial to determine the functional form of Equation (2), as well as to extract the constants, random variables, and develop the equivalent functional form that is shown in Equation (3). While the methods for the determination are described elsewhere [13, 35], they are presented briefly here. Initially, an artificial neural network containing the relevant input variables and output variable was developed, and interrogated to determine the 'virtual experiments', in which the influence of a single input variable on an output variable is assessed. Concurrently, a physically-based equation (see Equation (2)) is postulated, and an alternative machine learning strategy (here, genetic algorithms) are applied, and the optimized equation similarly interrogated with virtual experiments. When the virtual experiments are nominally identical, it can be said that the physically-based equation and best artificial neural

network are nominally equivalent. In this way, it is possible to learn physics from databases. This approach was first applied to wrought structures, and the resulting equation to predict the yield strength of Ti-6Al-4V has been found to be quite robust, and largely independent of the process by which the material is made. Equation (2) can be rewritten by substituting the appropriate constants, the random variables, and equivalent functional forms as follows:

$$\sigma_{YS} = \left\{ \begin{bmatrix} 89F_V^{\alpha} + 45(1-F_V^{\alpha}) + F_V^{\alpha}[149x_{Al}^{0.667} + 759x_O^{0.667}] \\ +(1-F_V^{\alpha})[\sqrt{22x_V^{0.7}} + \sqrt{235x_{Fe}^{0.7}}]^2 + 150F_V^{colony}\sqrt{t_{\beta-rib}/t_{\alpha-lath}} \\ +125F_V^{colony}/\sqrt{t_{colony}} + (t_{colony}/t_{\alpha-lath}) \\ +10^5(1-F_V^{colony})\alpha MG\sqrt{b/t_{\alpha-lath}} \end{bmatrix} \right\} F_V^{colony}(1-A_D), \quad (3)$$

where x_C is the composition for element C, α is a correction factor, M is the Taylor factor, G is the shear modulus, b is the Burgers vector, and A_D is the orientation debit which has the following values:

$$A_D = \begin{cases} 0.04 & \text{for } x, \\ 0.03 & \text{for } y, \\ 0.08 & \text{for } z, \\ -0.01 & \text{for } xc, \\ 0.04 & \text{for } zc. \end{cases} \quad (4)$$

This constitutive equation, (3) and (4), will be used to estimate and predict the yield stress of Ti-6Al-4V deposited by electron beam additive manufacturing to build the notional parts. The orientations x, y, and z in equation (4) take on the prototypical Euclidean directions, while xc and

zc refer to specimens where crosshatching was conducted between layers, resulting in different textures and thermal histories.

4. Simulation of Yield Stress Model

Using the model given in equations (3) and (4) and the cdfs for the random variables given in Table 1, Monte Carlo simulation was performed to analyze the model for σ_{YS}. Figure 6 shows all 78 of the data for σ_{YS} from NP1, NP2, and NP3, and superimposed upon them are colors to indicate the specific orientations. The number in parenthesis specifies the sample size for that orientation. The model estimate is σ_{YS} computed from equations (3) and (4) with the actual data for the appropriate material parameters observed for the 78 specimens. Clearly, the model estimate is quite good at capturing the central tendency of the σ_{YS} data; however, it is not as good in the upper and lower tails. This deviation in the tails may be due to the fact that averages in chemical composition and microstructure are used from nearby regions, as opposed to precise measurements of the material that undergoes yielding – an experimental limitation. The solid line is the simulation for the model; however, the value for A_D is assumed to be the weighted average of the values in equation (4). Thus, A_D is 0.05. Again, the simulation is quite good over the central tendency, and it is reasonably good in the upper tail. In the lower tail, however, it is not representative of the data. The blue lines correspond to confidence bounds using mean square error (MSE) and mean absolute error (MAE) analyses. Recall that for the error e_i is the difference between the model estimate and the data. The MSE is given by

$$MSE = \frac{1}{n}\sum_{i=1}^{n} e_i^2, \tag{5}$$

and the root mean square error (RMSE) is the square root of the MSE. For unbiased error distributions the standard error is equivalent to the RMSE [10]. If the mean of the error distribution is nonzero, an adjustment to correct for the bias is warranted [37]. Several authors, *e.g.*, see [38, 39], suggest that a better measure of the error is the MAE given by

$$MAE = \frac{1}{n}\sum_{i=1}^{n}|e_i|. \tag{6}$$

Both the RMSE and MAE are considered in the ensuing analyses. The ±2σ lines are approximately the 95% confidence bounds, where σ is the RMSE or the square root of the MAE. The MAE bounds on Figure 6 are tighter than the MSE bounds; however, neither adequately captures the lower tail of the experimental data.

Figure 7 is identical to Figure 6 with the addition of another simulation shown as the gray line for the z orientation. All of the cdfs for the random variables were estimated using only the data associated with the z orientation, and A_D is 0.08 for the *z* orientation. The cdfs and their parameters are given in Table 1. The only cdf that is significantly different is for x_{Fe}. There is not that much difference between the simulations using all the data and just the z orientation data. In the lower tail the difference in the two simulations is about 3 MPa. From a probability of about 0.1 to 0.5 the difference is about 5 MPa. The difference continues to grow up to over 20 MPa for probabilities greater than 0.99. Again, the simulation for the z orientation data is not that good in the lower tail. The confidence bounds are a bit tighter; however, they are still not acceptable for the lower tail data.

5. Data Fusion with Science Based Modeling

The effect of uncertainty is a critical aspect in modeling complex engineered structural materials, especially those in additive manufacturing. Uncertainty, which cannot be eliminated from manufacturing and modeling, must be adequately managed. Typically, limited data and information are available for new materials, designs, and manufacturing processes. A methodology is proposed to manage uncertainty. Here, uncertainty is assumed to include contributions from any and all sources. The proposed methodology was developed previously [29] and is used herein. The model in equations (3) and (4) is calibrated with experimental data. The methodology is based upon the premise that two cdfs $G(x)$ and $H(x)$ are of the same type if and only if there are constants $a > 0$ and b such that

$$G(ax+b) = H(x) \tag{7}$$

for all x; see [40].

The choices of a and b in equation (7) for this application are directly related to the experimental data for σ_{YS}. In fact, the goal is to integrate limited data with a reasonably accurate model to manage the associated uncertainties. As the sample size increases, accuracy of statistical estimation increases. For the current application, the sample size for σ_{YS} is $n = 78$, as shown on Figures 6 and 7, which is sufficiently large that the estimation will be quite good. In [29] it was shown that as few as 15 data used for the calibration yields acceptable results. Consequently, it is appropriate to use the methodology for the yield stress model. The experimental data for σ_{YS}, $\{x_j : 1 \le j \le n\}$, are used to calibrate the scientifically based model simulations to account for uncertainty. For optimal performance the data x_j should be from multiple heats and orientations

within the heats. This is exactly what is represented from the σ_{YS} data from NP1, NP2, and NP3, as these parts were built using different lots of material, on two different machines and under different process control conditions. The method of calibration is chosen so that the average and standard deviation of the calibrated model simulations match those for the σ_{YS} data. Let $\{y_j : 1 \le j \le N_s\}$ be the model simulations, where N_s is the number of simulations. The linear transformation of y_j into z_j is defined as

$$z_j = a y_j + b, \tag{8}$$

where

$$a = \frac{s_x}{s_y} \text{ and } b = \bar{x} - \frac{s_x}{s_y}\bar{y}, \tag{9}$$

where s_x and s_y are the standard deviations and $\bar{x}$ and $\bar{y}$ are the averages, respectively, for $\{x_j : 1 \le j \le k\}$ and $\{y_j : 1 \le j \le N_s\}$. Thus, the transformed, calibrated simulation is $\{z_j : 1 \le j \le N_s\}$. It should be noted that this transformation is consistent with equation (7). Specifically, the geometric effect of this transformation is that the model cdf computed using simulations is translated and rotated while the probabilities remain the same. Consequently, the method for the calibration will be designated as distribution translation and rotation (DTR).

Figure 8 shows all the σ_{YS} data and the model estimates, as before. The solid line is the DTR calibration of the simulation as described above. Notice that the DTR calibration is an excellent representation of the σ_{YS} data, except for three data. Also, the confidence bounds are very tight. If

the confidence bounds had been constructed using ±3σ, representing approximately 99% confidence, all the σ_{YS} data would be with the MSE bounds. Thus, the DTR calibration is an excellent representation of the σ_{YS} data. The reason for this is that the σ_{YS} data is collected from three different builds with three different chemistries and different orientations within the builds.

6. DTR Validation

The quality of the DTR calibration as shown in Figure 8 can be investigated by comparing it to another independent set of σ_{YS} data. Such data is available from a fourth build, NP4B. Consider Figure 9, where the σ_{YS} data from NP4B, with a sample size of 93, are shown. The eight different orientations are also highlighted with their corresponding sample sizes. The lower tail is comprised of eight σ_{YS} data from the z orientation. The most apparent observation is that the DTR calibration for the scientifically based model is an excellent representation for the NP4B σ_{YS} data. Importantly, the DTR calibration is identical to that shown on Figure 8. No alteration has been made to accommodate the NP4B σ_{YS} data. In this case, the MSE and MAE analyses are graphically indistinguishable. The approximate 95% confidence bounds entirely encompass the NP4B σ_{YS} data. The width of the confidence bounds is approximately 38 MPa which is about 5% of the estimated σ_{YS} from the DTR calibration. Thus, the DTR calibration is an excellent representation for the σ_{YS} data of the AMSR process.

7. DTR Calibration Prediction

Given that the DTR calibration is an excellent representation for σ_{YS} data, as shown in Figure 9, the DTR calibration can be refined further. Since there are σ_{YS} data from four builds, all the

available σ_{YS} data were used to recalibrate the DTR simulation. In passing, one of the best features of the DTR methodology is that it is iterative. As more data are available and as the scientifically based model is refined, the calibration can easily be updated. Figure 10 has the DTR prediction using the σ_{YS} data from all four builds to calibrate it. The prediction is an excellent representation of the 171 σ_{YS} data. In fact, the KS and AD goodness-of-fit tests indicate that it is acceptable for any significance level less than 25%. The MSE confidence bounds are quite tight, as well. In fact, the widths of the confidence bounds are 6.54 MPa and 9.81 MPa, respectively, which correspond to less than 1.3% of the estimated DTR σ_{YS} model. Only two data lie on the lower confidence bound. All the other data are well within the bounds. The lowest σ_{YS} data with a value of 772.2 MPa is from a y orientation specimen. The next smallest σ_{YS} data from a y orientation specimen is 837.7 MPa, which is graphically identical to values from 5 other orientations, all of which are covered by the zc orientations circle. The maximum σ_{YS} data for a y orientation specimen is 917.0 MPa. Thus, the smallest σ_{YS} data is about 65 MPa smaller than the second smallest. Although this σ_{YS} data may be correct, it does seem a bit out of the range of the expected σ_{YS} values for the y orientation. Even so, this value is not that far from the proposed DTR model for the σ_{YS}. Thus, the overall recommendation is that the DTR estimate in Figure 10 is appropriate for prediction of future AMSR σ_{YS} data. An additional comment that is appropriate at this time is that the DTR model is well-suited for estimation and prediction of the σ_{YS} outside the range of the laboratory conditions.

8. Conclusions

Strategically merging experimental data with scientifically based probability and statistical modeling has been shown to yield excellent results for the estimation of the yield stress of the directed energy deposition process used for the additive manufacturing specimens considered in this effort. The methodology also considers uncertainty from all sources, including those from modeling, experimentation, and the manufacturing process. Three aspects of the approach are critical. An accurate scientifically based model is essential because modeling deficiency is a major source of uncertainty. Sufficient data for characterization of the model variables are needed. For the example in this paper, there are nine random variables for which cdfs are needed. Also, experimental data for the yield stress are required for the calibration. The number of yield stress data for this effort was sufficiently large, including four different parts using different lots of material, different deposition machines, and different process control conditions. Thus, calibration of the model and validation of the methodology were achieved. Consequently, the proposed methodology has been shown to be extremely effective for modeling yield stress. No doubt, further refinements could be made; however, the approach seems to be quite sound. The adoption of the procedure is recommended.

ACKNOWLEDGEMENTS

This material is based upon work supported by the Defense Advanced Research Projects Agency under Contract No. HR0011-12-C-0035 (“An Open Manufacturing Environment for Titanium Fabrication”) and F33615-00-2-5216 (“Accelerated Insertion of Materials”). The views, opinions and/or findings expressed are those of the authors and should not be interpreted as representing the official views or policies of the Department of Defense or the U.S. Government.

REFERENCES

1. A.S. Wu, D.W. Brown, M. Kumar, G.F. Gallegos, W.E. King, An experimental investigation into additive manufacturing-induced residual stresses in 316L stainless steel, Metallurgical and Materials Transactions A 45:13 (2014) 6260-6270.

2. S.A. Khairallah, A.T. Anderson, A. Rubenchik, W.E. King, Laser powder-bed fusion additive manufacturing: Physics of complex melt flow and formation mechanisms of pores, spatter, and denudation zones, Acta Materialia 108 (2016) 36-45.

3. L. Adler, Z. Fu, C. Koerner, Electron beam based additive manufacturing of Fe3Al based iron aluminides–Processing window, microstructure and properties, Materials Science and Engineering: A (2020) 139369.

4. C. Körner, Additive manufacturing of metallic components by selective electron beam melting—a review, International Materials Reviews 61:5 (2016) 361-377.

5. M.R. Rolchigo, R. LeSar, Application of alloy solidification theory to cellular automata modeling of near-rapid constrained solidification, Computational Materials Science 163 (2019) 148-161.

6. R.R. Dehoff, M.M. Kirka, W.J. Sames, H. Bilheux, A.S. Tremsin, L.E. Lowe, S.S. Babu, Site specific control of crystallographic grain orientation through electron beam additive manufacturing, Materials Science and Technology 31:8 (2015) 931-938.

7. M.J. Bermingham, D.H. StJohn, J. Krynen, S. Tedman-Jones, M.S. Dargusch, Promoting the columnar to equiaxed transition and grain refinement of titanium alloys during additive manufacturing, Acta Materialia 168 (2019) 261-274.

8. D. Zhang, D. Qiu, M.A. Gibson, Y. Zheng, H. L. Fraser, D.H. StJohn, M.A. Easton, Additive manufacturing of ultrafine-grained high-strength titanium alloys, Nature 576:7785 (2019) 91-95.

9. J.H. Martin, B.D. Yahata, J. M. Hundley, J. A. Mayer, T.A. Schaedler, T.M. Pollock, 3D printing of high-strength aluminium alloys, Nature 549:7672 (2017) 365-369.

10. P.C. Collins, D.A. Brice, P. Samimi, I. Ghamarian, H.L. Fraser, Microstructural control of additively manufactured metallic materials, Annual Review of Materials Research 46 (2016) 63-91.

11. R. Banerjee, P.C. Collins, D. Bhattacharyya, S. Banerjee, H.L. Fraser, Microstructural evolution in laser deposited compositionally graded α/β titanium-vanadium alloys, Acta Materialia 51:11 (2003) 3277-3292.

12. J.J. Lewandowski, M. Seifi, Metal additive manufacturing: a review of mechanical properties, Annual review of materials research 46 (2016).

13. B. Hayes, B. Martin, B. Welk, S. Kuhr, T. Ales, A. Baker, C.V. Haden, D.G. Harlow, H.L. Fraser, P.C. Collins, Predicting Tensile Properties of Ti-6Al-4V Produced Via Directed Energy Deposition, Acta Mater. 133 (2017) 120-133.

14. R. Banerjee, D. Bhattacharyya, P.C. Collins, G.B. Viswanathan, H.L. Fraser, Precipitation of grain boundary α in a laser deposited compositionally graded Ti–8Al–xV alloy–an orientation microscopy study, Acta Materialia 52:2 (2004) 377-385.

15. A.R. Reichardt, P. Dillon, J.P. Borgonia, A.A. Shapiro, B. W. McEnerney, T. Momose, P. Hosemann, Development and characterization of Ti-6Al-4V to 304L stainless steel

gradient components fabricated with laser deposition additive manufacturing, Materials & Design 104 (2016) 404-413.

16. L. Yan, Y. Chen, F. Liou, Additive manufacturing of functionally graded metallic materials using laser metal deposition, Additive Manufacturing 31 (2020) 100901.

17. C. Zhang, F. Chen, Z. Huang, M. Jia, G. Chen, Y. Ye, Y. Lin, W. Liu, B. Chen, Q. Shen, L. Zhang, Additive manufacturing of functionally graded materials: A review, Materials Science and Engineering: A 764 (2019), 138209.

18. S. Nag, R. Banerjee, H.L. Fraser, A novel combinatorial approach for understanding microstructural evolution and its relationship to mechanical properties in metallic biomaterials, Acta Biomaterialia 3:3 (2007) 369-376.

19. M.J. Matthews, G. Guss, S.A. Khairallah, A.M. Rubenchik, P.J. Depond, W.E. King, Denudation of metal powder layers in laser powder bed fusion processes, Acta Materialia 114 (2016) 33-42.

20. A.A. Martin, N.P. Calta, S.A. Khairallah, J.Wang, P.J. Depond, A.Y. Fong, V.Thampy, G.M. Guss, A.M. Kiss, K.H. Stone, C.J. Tassone, Dynamics of pore formation during laser powder bed fusion additive manufacturing, *Nature communications* 10:1 (2019) 1-10.

21. C.L.A. Leung, S. Marussi, R.C. Atwood, M. Towrie, P.J. Withers, P.D. Lee, In situ X-ray imaging of defect and molten pool dynamics in laser additive manufacturing, Nature communications 9:1 (2018) 1-9.

22. N.D. Parab, C. Zhao, R. Cunningham, L.I. Escano, K. Fezzaa, W. Everhart, A.D. Rollett, L. Chen, T. Sun, Ultrafast X-ray imaging of laser–metal additive manufacturing processes, Journal of synchrotron radiation 25:5 (2018) 1467-1477.

23. Z. Wang, A.D. Stoica, D. Ma, A.M. Beese, Stress relaxation behavior and mechanisms in Ti-6Al-4V determined via in situ neutron diffraction: Application to additive manufacturing, Materials Science and Engineering: A 707 (2017) 585-592.

24. N. Parab, C. Zhao, R. Cunningham, L.I. Escano, K. Fezzaa, A. Rollett, L. Chen, T. Sun, In situ Characterization of Laser Powder Bed Fusion Using High-Speed Synchrotron X-ray Imaging Technique, Microscopy and Microanalysis 25:S2 (2019) 2566-2567.

25. H. Taheri, M.R.B.M. Shoaib, L.W. Koester, T.A. Bigelow, P.C. Collins, L.J. Bond, Powder-based additive manufacturing-a review of types of defects, generation mechanisms, detection, property evaluation and metrology, International Journal of Additive and Subtractive Materials Manufacturing 1:2 (2017) 172-209.

26. J.L. McNeil, K. Sisco, C. Frederick, M. Massey, K. Carver, F. List, C. Qiu, M. Mader, S. Sundarraj, S.S. Babu, In-Situ Monitoring for Defect Identification in Nickel Alloy Complex Geometries Fabricated by L-PBF Additive Manufacturing, Metallurgical and Materials Transactions A 51:12 (2020) 6528-6545.

27. E.A. Lindgren, US Air Force perspective on validated NDE–Past, present, and future, AIP Conference Proceedings, 1706: 1, p. 020002. AIP Publishing LLC, 2016.

28. J.C. Aldrin, E.A. Lindgren, The need and approach for characterization-US air force perspectives on materials state awareness, *AIP Conference Proceedings*, 1949:1, p. 020004. AIP Publishing LLC, 2018.

29. D.G. Harlow, Probabilistic Property Prediction, Eng. Fract. Mech. 74 (2007) 2943-2951.

30. A. Baker, P.C. Collins, J.C. Williams, New Nomenclatures for Heat-Treatments of Additively Manufactured Titanium Alloys, JOM 69 (2017) 1221-1227.

31. S. Kar, T. Searles, E. Lee, G.B. Viswanathan, H.L. Fraser, J. Tiley, R. Banerjee, Modeling the Tensile Properties in β-processed α/β Ti Alloys, Metall. Mater. Trans. A 37 (2006) 559-566.

32. Collins PC, Koduri S, Welk B, Tiley J, Fraser HL. Metall Mater Trans A 2013; 44:1441.

33. P.C. Collins, C.V. Haden, I. Ghamarian, B.J. Hayes, T. Ales, G. Penso, V. Dixit, and D.G. Harlow, Progress Toward an Integration of Process-Structure-Property-Performance Models for "Three-Dimensional (3-D) Printing" of Titanium Alloys, JOM, 66 (2014) 1299-1309.

34. C.V. Haden, P.C. Collins, and D.G. Harlow, Yield Strength Prediction of Titanium Alloys, JOM, 67 (2015) 1357-1361.

35. Ghamarian, I, Hayes B, Samimi P, Welk BA, Fraser HL, Collins PC. Mater Sci Eng A 2016; 660:172.

36. W.Q. Meeker, L.A. Escobar, Statistical Methods for Reliability Data. New York: Wiley; 1998.

37. Chai T Draxler RR. Geosci Model Dev 2014; 7:1247.

38. Willmont C. Matsuura K. Clim Res 2005; 30:79.

39. Willmont CJ, Matsuura K, Robeson, SM. Atmos Environ 2009; 43:749.

40. R.E. Barlow, F. Proschan, Statistical Theory of Reliability and Life Testing: Probability Models. Silver Springs, MD: To Begin With; 1981.

Table 1. Statistically estimated random variables for materials data from NP1, NP2, and NP3.

random variable	cdf	parameter	parameter	parameter
Al concentration	Normal	$\mu = 5.697$	$\sigma = 0.131$	
V concentration	Normal	$\mu = 4.228$	$\sigma = 0.241$	
Fe concentration	Discrete	min = 0.161	max = 0.177	p(Fe) = 0.39
O concentration	Discrete	min = 0.165	max = 0.169	p(O) = 0.73
alpha volume fraction	Normal	$\mu = 0.901$	$\sigma = 0.021$	
colony volume fraction	Normal	$\mu = 0.178$	$\sigma = 0.104$	
alpha lath width	Normal	$\mu = 1.10$ μm	$\sigma = 0.23$ μm	
beta rib width	Normal	$\mu = 0.119$ μm	$\sigma = 0.023$ μm	
colony scale factor	Weibull	$\rho = 1.48$	$\beta = 4.28$ μm	$\gamma = 3.23$ μm

Figure 1. Electron beam additive manufacturing notional part; top (left) and bottom (right).

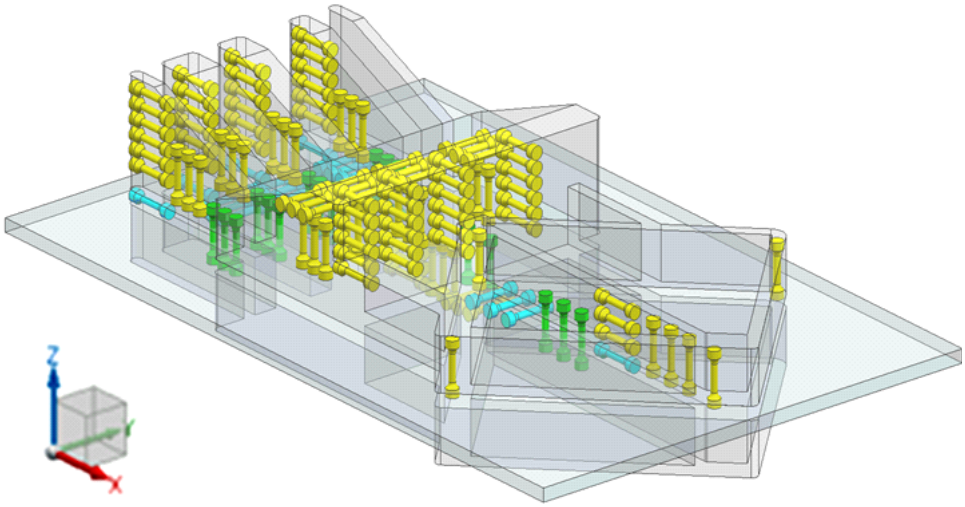

Figure 2. Schematic of tensile specimens machined from notional part.

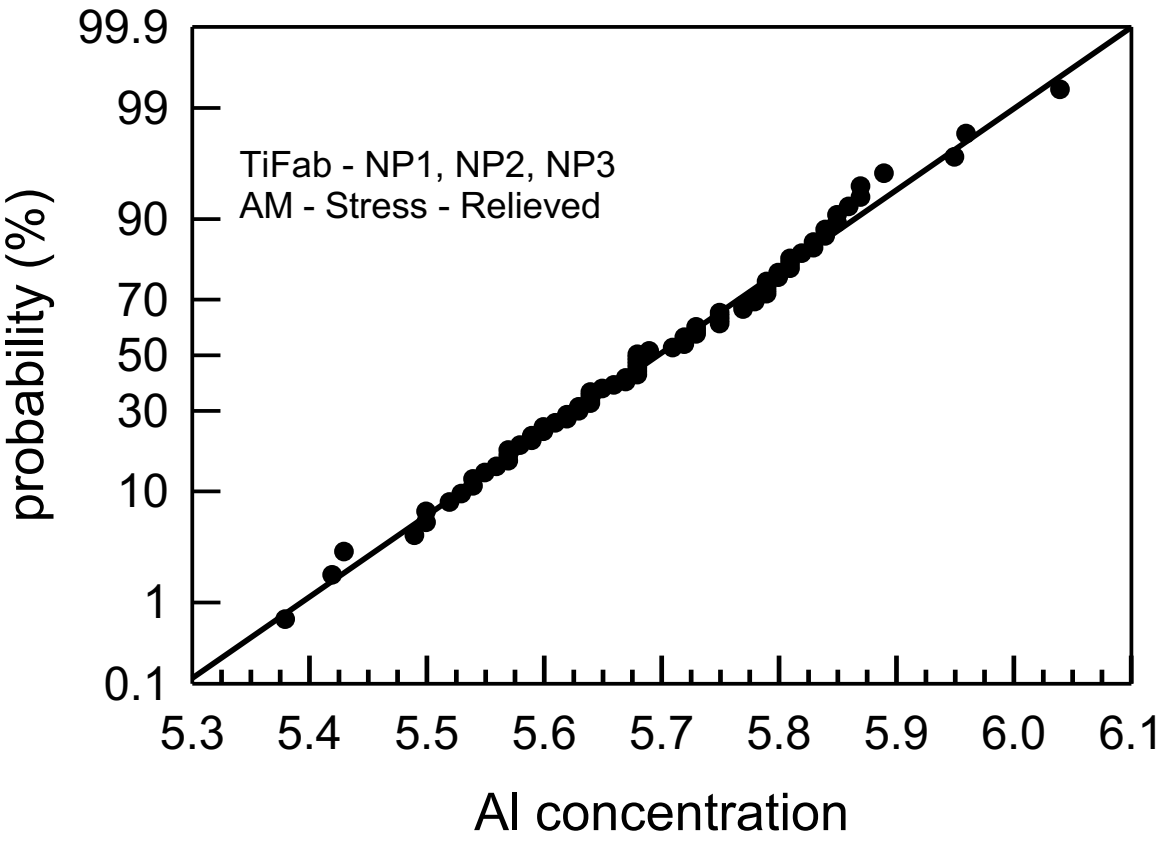

Figure 3. Al concentration for NP1, NP2, and NP3.

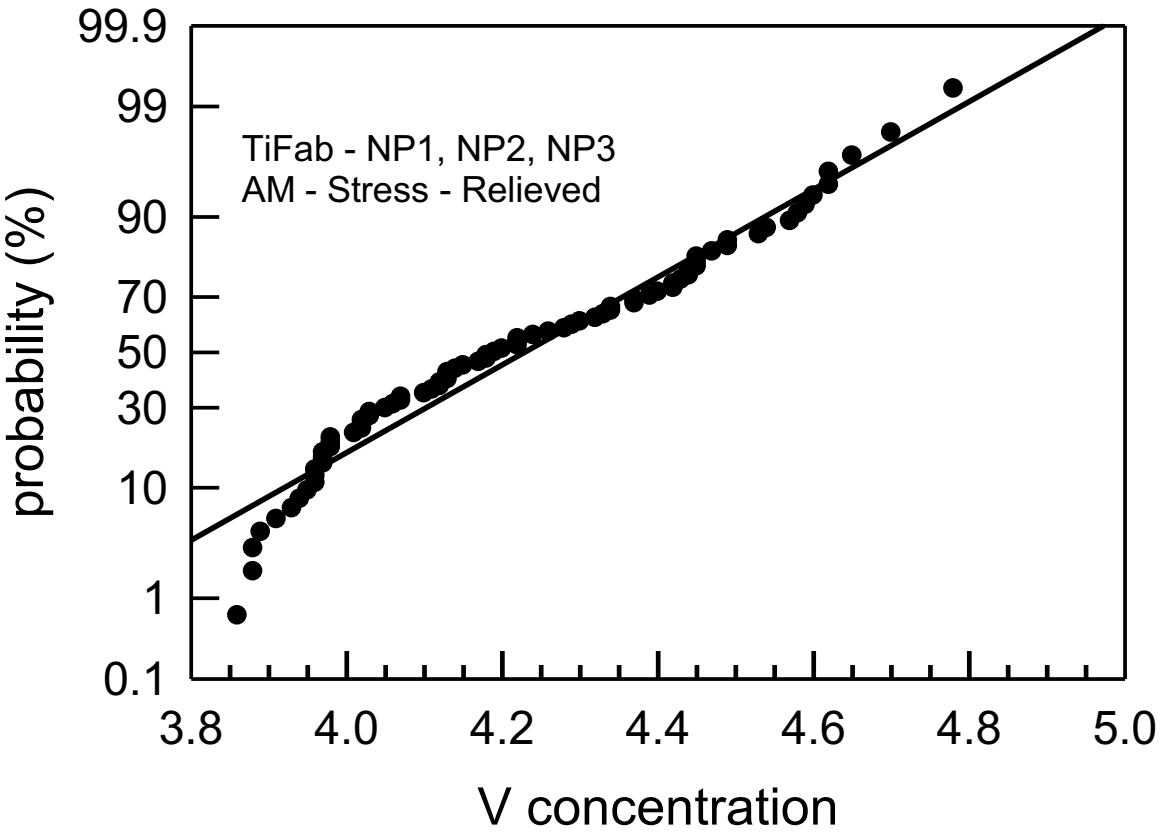

Figure 4. V concentration for NP1, NP2, and NP3.

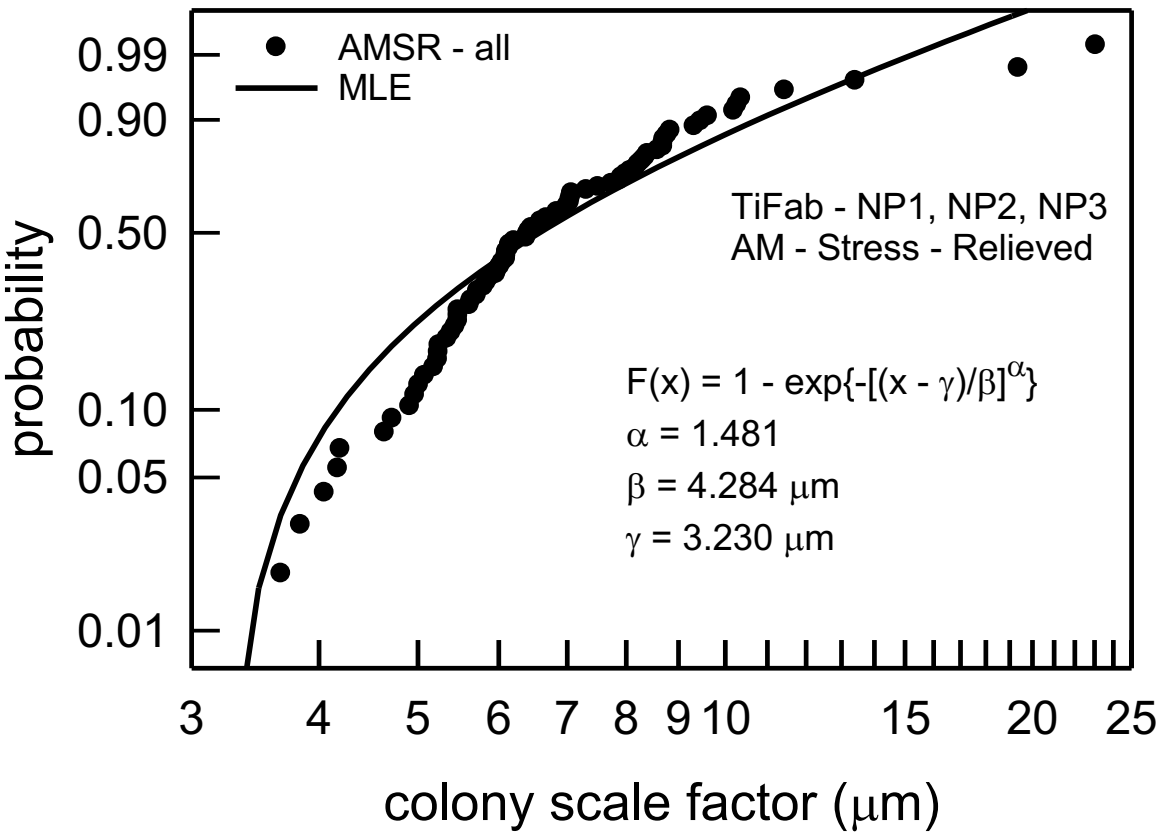

Figure 5. Colony scale factor for NP1, NP2, and NP3.

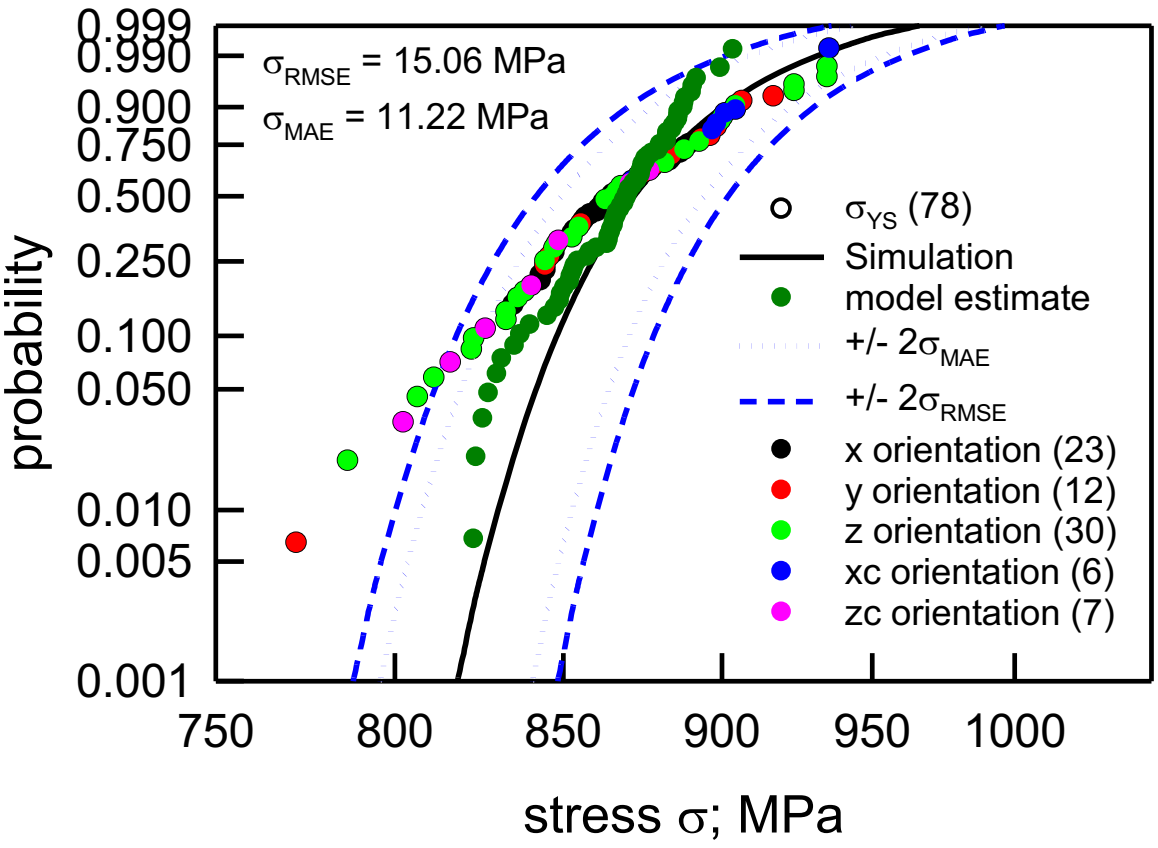

Figure 6. Yield stress model and data for NP1, NP2, and NP3.

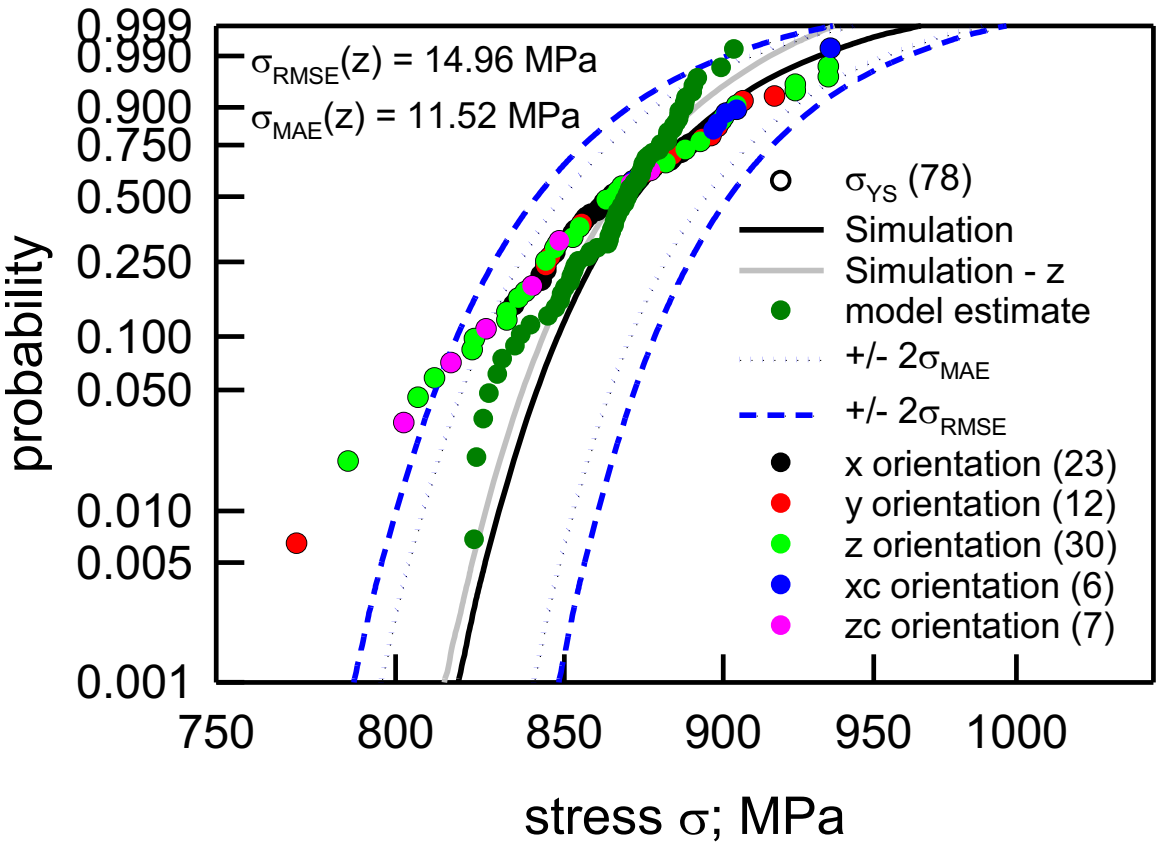

Figure 7. Yield stress model for all data and z orientation data for NP1, NP2, and NP3.

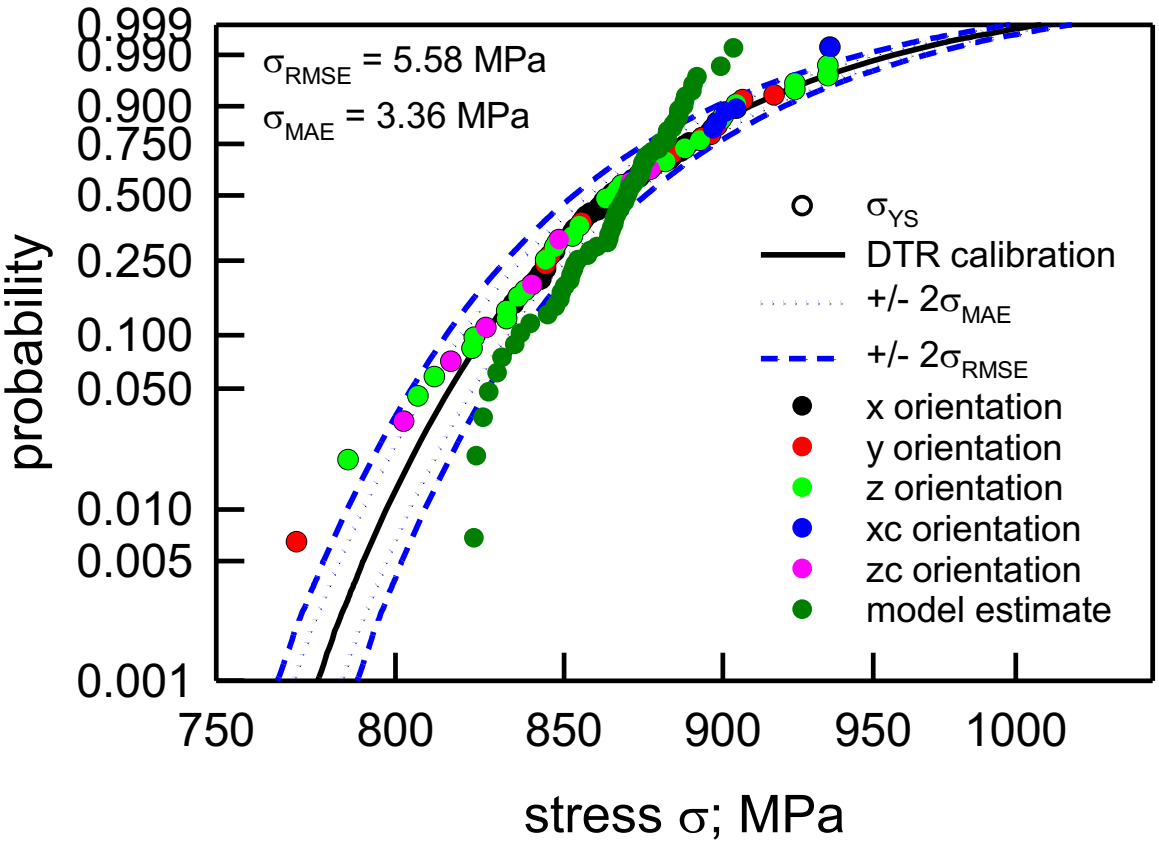

Figure 8. DTR calibrated yield stress model for all data for NP1, NP2, and NP3.

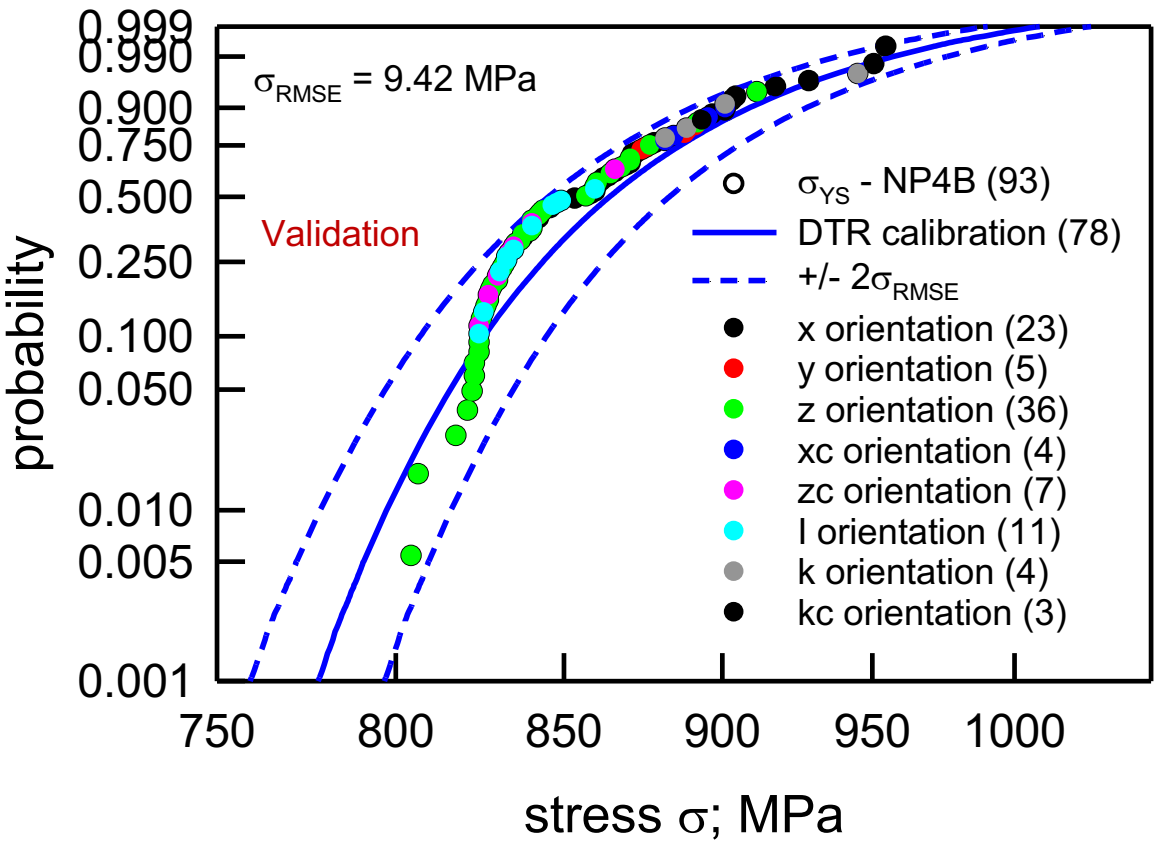

Figure 9. Validation of DTR calibrated yield stress model with data from NP4B.

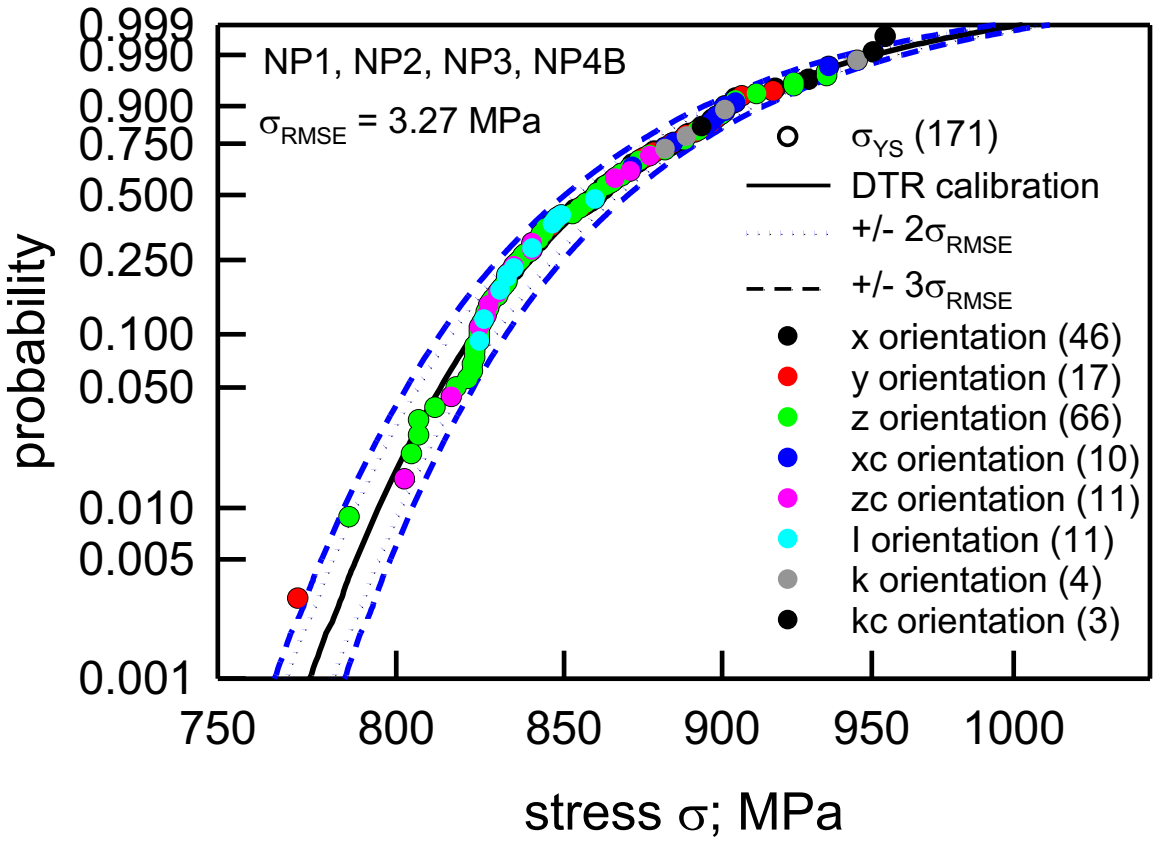

Figure 10. DTR calibrated yield stress model with data from NP1, NP2, NP3, and NP4B.